Mechanisms behind Seasonal Differences in the Recent Interdecadal Change in Tropical Cyclone Genesis Frequency over the Western North Pacific

JINHUI JU,[a] DOO-SUN R. PARK,[a,b,c] DASOL KIM,[d] MINHEE CHANG,[e] CHANG-KYUN PARK,[f] JONG-SEONG KUG,[g] AND DAEOK YOUN[h]

[a] *BK21 Weather Extremes Education & Research Team, Department of Atmospheric Sciences, Kyungpook National University, Daegu, South Korea*
[b] *Department of Earth Science Education, Kyungpook National University, Daegu, South Korea*
[c] *Center for Atmospheric REmote sensing, Kyungpook National University, Daegu, South Korea*
[d] *Department of Environmental Engineering, Seoul National University of Science and Technology, Seoul, South Korea*
[e] *Environmental Planning Institute, Graduate School of Environmental Studies, Seoul National University, Seoul, South Korea*
[f] *AVEL Solution Development Team, LG Energy Solution, Seoul, South Korea*
[g] *School of Earth and Environmental Sciences, Seoul National University, Seoul, South Korea*
[h] *Department of Earth Science Education, Chungbuk National University, Cheongju, South Korea*

(Manuscript received 29 October 2024, in final form 26 March 2025, accepted 11 April 2025)

ABSTRACT: In the late 1990s, tropical cyclone genesis over the western North Pacific (WNP) abruptly decreased, with seasonality that is significant only from October to December (OND). A previous study suggested that this seasonality can be attributed to the seasonal location of anomalous anticyclonic flow in the WNP, which are associated with increased precipitation over the seasonal concentrated rainfall regions (SCRRs) within the Indo-Pacific Ocean under La Niña–like SST warming, which conforms to the "rich-get-richer" mechanism. However, this argument has not been explicitly verified. Here, by using dynamic models, i.e., the Model for Prediction Across Scales-Atmosphere (MPAS-A) and the linear baroclinic model (LBM), we sought to validate the argument. Using the MPAS-A, we implemented two experiments, respectively, forced by the global daily climatological SST and by the La Niña–like SST warming. The results showed that the increased precipitation over the SCRRs corresponds closely to the rich-get-richer mechanism. However, the MPAS-A experiments poorly mimicked observed precipitation changes in the central to eastern Pacific, possibly because they are less sensitive to slightly warmer SSTs. The LBM experiments showed that the diabatic heating rates induced by tropical rainfall anomalies not only in the Indo-Pacific warm pool but also in the central to eastern Pacific were significant factors in the formation of the anomalous anticyclones over the WNP in OND. Hence, changes in diabatic heating rates in both basins, induced by the increase in precipitation, can contribute to the seasonality of changes in the large-scale circulation over the WNP.

KEYWORDS: Tropical cyclones; Decadal variability; Interdecadal variability

1. Introduction

In recent decades, there has been an abrupt decrease in tropical cyclone genesis frequency (TCGF) over the western North Pacific (WNP) since the mid-1990s (He et al. 2015; Hong et al. 2016; Liu and Chan 2013; Park et al. 2011; Zhao et al. 2018b). The change exhibits seasonality (Chang et al. 2021; Hsu et al. 2014; Liu et al. 2019; Shan and Yu 2020; Zhao and Wang 2016), with the significant decrease only seen in the late season [October–December (OND)]. Liu et al. (2019) investigated changes in TCGF over the WNP during the 1979–2012 period and found significant reductions during OND, with the largest decline in October. Additionally, Hsu et al. (2014) showed that during the 1979–2011 period, the TCGF in OND significantly decreased by about 2.7. Zhao and Wang (2016) and Chang et al. (2021) found that the TCGF has decreased significantly in OND since 1998, which is the year known for the climate regime shift in the Pacific Ocean (Hong et al. 2014; McPhaden et al. 2011; Zhao et al. 2018a).

A larger proportion of tropical cyclones (TCs) intensify into strong TCs in autumn than in summer, though the annual average TCGF in autumn is less than that in summer (Deng et al. 2021; Hsu et al. 2014). Deng et al. (2021) reported that from 1979 to 2017, 39.5% of typhoons in autumn developed into the super typhoon category, in which the maximum wind speed exceeds 51 m s^{-1}, while only 25.5% become super typhoons in summer. Most of the catastrophic typhoons in history, such as Tip (1979), Megi (2010), and Haiyan (2013), which caused significant loss of life and economic damage in East Asia, have occurred in autumn. Typhoon Tip struck Japan in October 1979, claiming 99 lives, and Typhoon Megi, striking in October 2010, caused enormous economic damage in East Asian countries, especially in the Philippines, where it killed more than 200 people. Typhoon Haiyan was especially disastrous, wreaking more than $2 billion in economic damages and killing over 6000 in the Philippines. Thus, understanding TC activity in the late season and the related mechanisms is very important.

Supplemental information related to this paper is available at the Journals Online website: https://doi.org/10.1175/JCLI-D-24-0604.s1.

Corresponding author: Doo-Sun R. Park, dsrpark@knu.ac.kr

DOI: 10.1175/JCLI-D-24-0604.1

The development of TCs is strongly affected by large-scale environmental fields (Baik and Paek 2001; Gray 1968; Murakami and Wang 2010; Park et al. 2011, 2017). Gray (1968) was the first study to propose a link between the development of TCs and large-scale environmental variables, which can be divided into dynamic factors, such as vertical wind shear (VWS) and lower-level relative vorticity, and thermodynamic factors, such as sea surface temperature (SST), static stability, and midlevel relative humidity. The TCs over the WNP are more influenced by dynamic factors (Chang et al. 2021; Liu and Chan 2013; Park et al. 2017; Sharmila and Walsh 2017; Wu et al. 2020). Sharmila and Walsh (2017) analyzed thermodynamic variables along with dynamic variables. By comparing high-TC years to low-TC years, they found that, in the WNP, thermodynamic factors were relatively unfavorable for the development of TCs during high-TC years, while all dynamic factors were more favorable.

Although oceanic thermodynamic conditions have weaker one-to-one relationship with TCGF, the spatial distribution of tropical SSTs strongly modulate dynamic conditions over the WNP (Guo et al. 2020; Lian et al. 2018; Sohn et al. 2013; Zhao and Allen 2019). The factors modulating the TCGF over the WNP, including low-level vorticity and midlevel humidity, can be mediated not only by SST over the WNP but also by SST over the tropical Indian Ocean and tropical Atlantic (Cao et al. 2016; Huo et al. 2015; Yu et al. 2016a,b). Cao et al. (2016) suggested that boreal spring SST anomalies over the tropical North Atlantic affect the TC activity over the WNP in the following summer and fall since the late 1980s. Yu et al. (2016b) elaborated that the first leading SST modes of tropical North Pacific, Indian Ocean, and North Atlantic are contributed to TCGF variability. Specifically, they elaborated that the first SST mode of the North Pacific accounted for 22%, while that of the North Atlantic accounted for 14.5%. In recent decades, SST in the tropical Pacific Ocean have become warmer in the west and relatively cooler in the east, which is referred to as the La Niña–like warming (An et al. 2012; Karnauskas et al. 2009). This zonal gradient in SST strengthens the Walker circulation, leading to stronger easterlies over the tropical WNP (Lian et al. 2018; Sohn et al. 2013; Zhao and Allen 2019). Enhanced easterlies could lead to larger meridional wind gradients in the tropics, which in turn cause the formation of anomalous anticyclones with stronger VWS, which are ultimately unfavorable for TC development (Choi et al. 2015; Hong et al. 2016; Hsu et al. 2014; Huangfu et al. 2018; Park et al. 2013).

This La Niña–like SST warming pattern has been suggested as a main cause of the recent decrease in TCGF by many previous studies (Hsu et al. 2014; Huangfu et al. 2018; Liu and Chan 2013; Park et al. 2013; Yu et al. 2016b; Zhang et al. 2018). However, the La Niña–like SST warming pattern does not show seasonality (Chang et al. 2021; Kohyama et al. 2017; Kosaka and Xie 2013; Zhang et al. 2011), so it cannot explain the seasonality of the change of TCGF. Recently, Chang et al. (2021) proposed the seasonally different locations of the climatological concentrated rainfall region within the Indian and the western Pacific oceans as a possible factor explaining this seasonality. They found that those high rainfall areas vary seasonally and that the strongest is located further west during OND than during the rest of the year. They suggested that convection has intensified in those high rainfall regions due to the La Niña–like SST warming, which is in accordance with the "rich-get-richer mechanism" described by Chou and Neelin (2004). Anomalous anticyclones could then be induced to the east of the intensified convective regions. Since the high rainfall region is located further west during OND, the anomalous anticyclones could be driven across the seasonal main development regions (MDRs) of TCs over the WNP only during this season, resulting in a significant reduction in TCGF.

The hypothesis suggested by Chang et al. (2021), however, has not been directly verified by model experiments to see if the rich-get-richer mechanism is valid under the La Niña–like SST warming pattern. In addition, they did not show dynamic causality, i.e., whether differences in diabatic heating imposed in the troposphere can induce the observed changes in large-scale circulations in the seasonal MDRs of the WNP, and they focused on diabatic heating only in the Indian and western Pacific regions, despite evidence supporting the contribution of decadal variability in the oceanic environment of the central and eastern Pacific on the Indo-Pacific warm pool convection (Han et al. 2017).

This study has two main objectives. First, we verify whether convection increases in the climatological concentrated rainfall regions under the La Niña–like SST warming pattern, i.e., whether the rich-get-richer mechanism is applicable, using models. Second, we investigate whether the observed diabatic heating within the central to eastern Pacific, as well as within the Indo-Pacific warm pool, can drive the seasonality of the large-scale circulation seen over the seasonal MDRs of the WNP. The rest of this study is organized as follows. In section 2, the data and methods are described, including a description of the model and setup. Section 3 presents the observed changes in the TCGF and large-scale circulation patterns and compares them with the findings of Chang et al. (2021). In section 4, the experimental design and the model results are presented and discussed, and we conclude with a summary and discussion in section 5.

2. Data and methods

a. TC data

We used the TC best track data from the Joint Typhoon Warning Center (JTWC) to analyze the seasonal long-term changes in the TCGF over the WNP (0°–40°N, 100°E–180°) during the period 1982–2020. This dataset provides TC information at 6-h intervals, including the TC center location in latitude and longitude, the maximum 1-min sustained wind speed in knots, the minimum sea level pressure in hectopascal, and the intensity classification, which includes tropical depression (TD), tropical storm (TS), typhoon (TY), and extrapolated (ET). In this study, TC genesis is defined as the point at which a TC first reaches tropical storm intensity or above, corresponding to a maximum 1-min sustained wind speed of at least 34 kt (1 kt $\approx$ 0.51 m s^{-1}). Using this dataset,

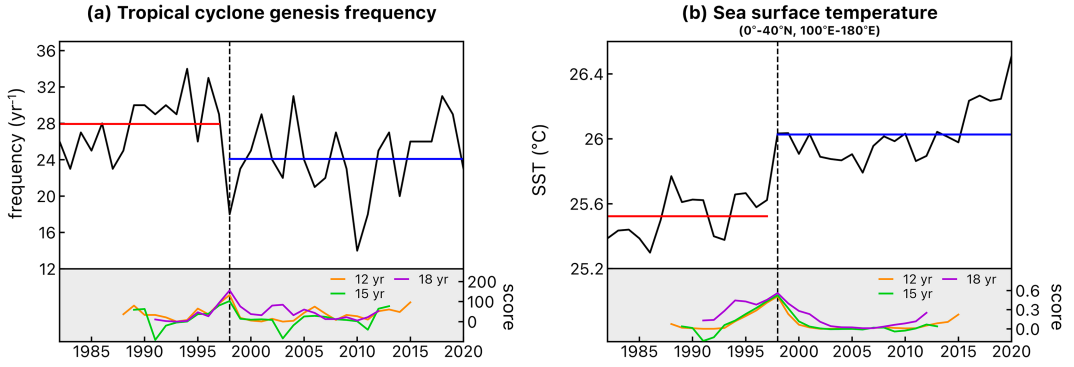

FIG. 1. Time series (black lines) of (a) TCGF and (b) SST over the WNP. Red and blue horizontal lines indicate the mean values for the period before and after the changepoint, i.e., 1998, respectively. The sliding window changepoint detection scores with window sizes of 12 (orange), 15 (green), and 18 (purple) years are shown, respectively.

we conducted sliding window changepoint analyses with window sizes of 12, 15, and 18 years, which confirmed an abrupt change in TCGF and SST around 1997/98 over the WNP (Fig. 1). Consequently, we divided the analysis period into early (1982–97) and recent (1998–2020) periods, which is consistent with the methodologies used in previous studies (Chang et al. 2021; Hsu et al. 2014; Zhao and Wang 2016). To investigate seasonal differences, we grouped the seasons into January–March (JFM), April–June (AMJ), July–September (JAS), and OND. This classification aligns with previous study, which have identified three periods for general circulation and TCGF characteristics: May–June, July–September, and October–December (Huang et al. 2011). Additionally, we examined the best track data from the Regional Specialized Meteorological Center (RSMC) and compared it with the JTWC dataset to identify inconsistencies in intensity between the datasets (Kossin et al. 2007). The results indicate that both datasets are consistent throughout the study period (cf. Table 1 and Table S1 in the online supplemental material).

The overlap gridding method (Chang et al. 2021; Kim et al. 2010; Park et al. 2013) was utilized to examine interdecadal changes in the spatial distribution of TCGF. Since each TC genesis location is represented as a point on the map, the spatial distribution is sensitive to one point. To avoid this problem, we counted over the grid boxes centered on the location of each TC genesis. The location of each TC genesis is binned into a 10° × 10° grid box centered on the genesis point on a map with a resolution of 2.5° × 2.5° latitude–longitude grid. The grids of the map within the 10° × 10° grid box were counted as one TC genesis for each TC. This method produced gridded TC genesis data with a 2.5° × 2.5° horizontal resolution from the genesis points (latitude–longitude) of the raw data. For example, the horizontal distribution of the annual-mean TCGF is shown in Fig. S1.

b. *Environmental field data*

The National Oceanic and Atmospheric Administration (NOAA) daily Optimum Interpolation Sea Surface Temperature (OISST), version 2.0, dataset, with a horizontal resolution of 0.25°, was used to investigate the seasonal long-term changes in SST and to prescribe the SST forcing in our model experiments (Reynolds et al. 2007). The monthly precipitation dataset was obtained from the Global Precipitation Climatology Project (GPCP), version 2.3, which has a horizontal resolution of 2.5° (Adler et al. 2018). The GPCP dataset was used to examine the climatology and long-term changes in precipitation. In the present study, the regions where the annual-mean precipitation is 6 mm day^{-1} or more are identified as climatological seasonal concentrated rainfall regions (SCRRs). For analysis of large-scale atmospheric fields (i.e., horizontal wind, relative vorticity at 850 hPa, and relative humidity at 700 hPa), we used the fifth major global reanalysis produced by the European Centre for Medium-Range Weather Forecasts (ERA5) monthly and 6-hourly data, which have 37 vertical levels and a horizontal resolution of 0.25° (Hersbach et al. 2020). While we used the monthly data bilinearly interpolated into 2.5° for analyzing the spatial distribution of atmospheric fields, the original 6-hourly data were used as initial conditions for the models.

TABLE 1. Seasonal average TCGFs over the WNP during the early and the recent periods, their difference, and the p value of the difference, as determined via the Student's t test. Values out of parentheses are derived from JTWC best track data, and those in parentheses are derived from RSMC best track data.

Season	Early period (1982–97)	Recent period (1998–2020)	Difference (recent minus early)	p value
JFM	0.9 (1.0)	1.1 (0.9)	+0.3 (−0.1)	0.45 (0.81)
AMJ	3.5 (3.5)	3.3 (3.2)	−0.2 (−0.3)	0.72 (0.66)
JAS	14.9 (15.1)	13.4 (13.6)	−1.5 (−1.6)	0.11 (0.11)
OND	8.6 (8.2)	6.3 (6.2)	−2.3 (−2.0)	<0.01 (0.01)

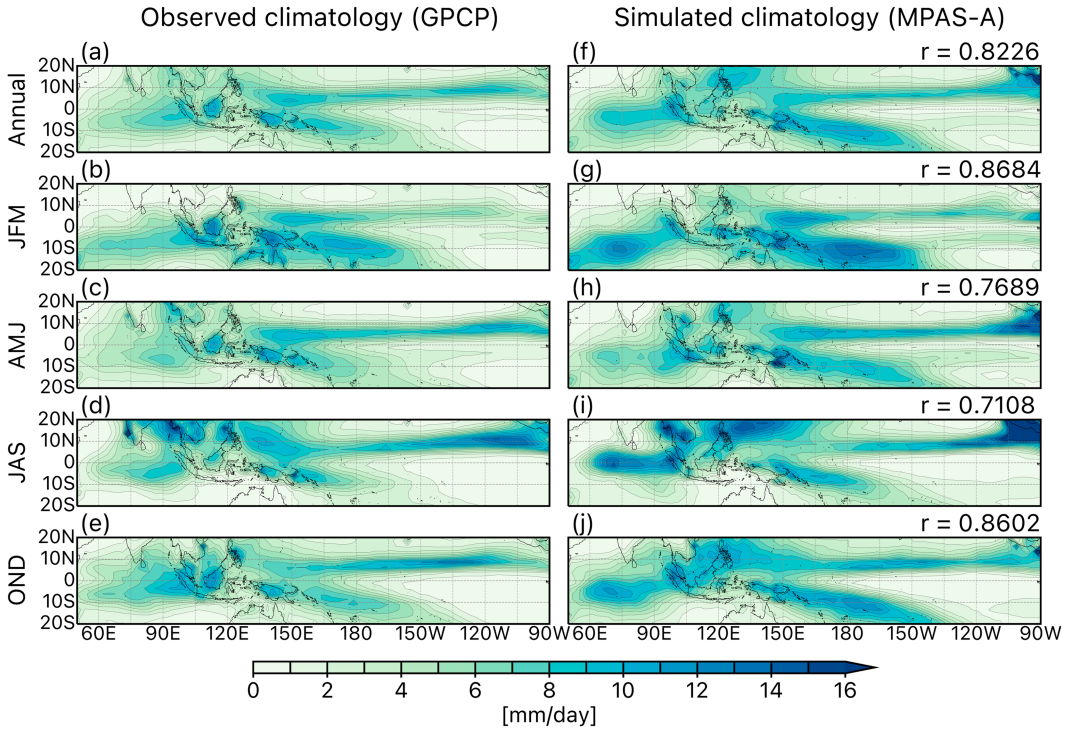

FIG. 2. Annual- and seasonal-mean precipitation of (a)–(e) GPCP and (f)–(j) CTRL run experiment from MPAS-A. (top-right second column) The *r* values denote the pattern correlation between the observed and simulated precipitation climatology within the tropical Indian and the tropical Pacific Oceans (20°S–20°N, 60°E–90°W), as determined via Pearson's *r* correlation analyses.

c. *Model description and setup*

The Model for Prediction Across Scales-Atmosphere (MPAS-A), version 7.3, was adopted for this study. MPAS-A is a nonhydrostatic and fully compressible atmospheric model provided by the National Center for Atmospheric Research (NCAR), and it satisfies the conservation of mass in dry air and other physical quantities. MPAS-A consists of a mesh-like grid system based on unstructured spherical centroidal Voronoi tessellations (SCVTs) (Ringler et al. 2008; Skamarock et al. 2012). These SCVTs are composed of two types of random cells constructed according to the Voronoi diagram and the Delaunay triangulations (C-grid staggering) and have a quasi-uniform shape (Ringler et al. 2010). The Cartesian coordinates are in a hybrid coordinate where terrain effects are smoothed with altitude, as suggested by Klemp (2011). The physical parameterizations in MPAS-A are a subset of those in the Advanced Research version of the Weather Research and Forecasting (WRF-ARW) Model.

In this study, we conducted global simulations with a horizontal resolution of 240 km and a vertical resolution of 55 layers, the upper bound of which reaches 30 km. In addition, the Grell–Freitas scheme (Grell and Freitas 2014) was applied for cumulus parameterization, and the WRF single-moment 6-class scheme (Hong and Lim 2006) was used for the microphysics. The Noah land surface (Niu et al. 2011) and the Mellor–Yamada–Nakanishi–Niino schemes (Nakanishi and Niino 2009) were applied for surface and boundary layer parameterizations, respectively. The Xu–Randall scheme (Xu and Randall 1996) was utilized for cloud fraction for radiation, and the Yonsei University scheme (Shin et al. 2010) was used for gravity wave drag by orography. These settings for the physical parameterizations were adopted based on the reasonable agreement between the horizontal patterns of simulated precipitation climatology they produced and those of the observed precipitation climatology from GPCP over the tropical Indian and Pacific Oceans (20°S–20°N, 60°E–90°W) (Fig. 2). Note, however, that there are still discrepancies, such as overestimated rainfall, that can be attributed to the inherent limitations of the model simulation.

MPAS-A was used to identify whether the precipitation in the SCRRs within the tropical Indian and Pacific Oceans is enhanced under the La Niña–like SST warming (i.e., the rich-get-richer mechanism). We conducted a control (CTRL) simulation and the experimental simulation, which was forced by the tropical SST changes. The SST field was updated daily throughout the simulations. The same SST pattern was prescribed each year for a total of 30 years, with the first 5 years excluded from analysis as a spinup period. Identical initial atmospheric conditions from ERA5 were applied to both simulations. Details of the forcing in the MPAS-A experiments will be given in section 4.

To investigate the causal relationship between the large-scale circulation over the WNP and the diabatic heating induced by precipitation anomalies within the Indian and Pacific

Oceans, we utilized the dry linear baroclinic model (LBM) (Watanabe and Kimoto 2000). LBM is usually used to evaluate the effects of individual forcings (e.g., SST, adiabatic heating) on synoptic-scale circulation and the causal relationships between them, including teleconnection (Annamalai 2010; Jin et al. 2006; Kosaka et al. 2009; Lu and Lin 2009; Yoo et al. 2012). It consists of linear atmospheric dynamic equations derived from the primitive equations presented in Watanabe and Kimoto (2000), with variables comprising vorticity, divergence, temperature, and the logarithm of surface pressure (Watanabe and Jin 2003).

In this study, the horizontal resolution of LBM was set to T42 (64 × 128) and the vertical resolution to 20 sigma levels. Atmospheric fields, such as zonal and meridional wind, temperature, specific humidity, and surface pressure, seasonally averaged from 1982 to 2020, were used as initial conditions for each experiment. Following the equation in Holton and Hakim (2013) and Hu and Duan (2015), the condensational diabatic heating (H, K day^{-1}) is calculated from the precipitation anomalies (P, mm day^{-1}) as follows:

$$H = \frac{P \times \rho_w \times L_c}{C_p \times (p_s/g)} \times 10^{-3} (\mathrm{K\,day^{-1}}),$$

where ρ_w is the average water density (1000 kg m^{-3}), L_v is the average latent heat of condensation (2.5 × 10^6 J kg^{-1}), C_p is the specific heat at constant pressure (1004 J kg^{-1} K^{-1}), p_s is the average surface pressure (101 325 Pa), and g is the average gravitational acceleration (9.806 65 m s^{-2}). Diabatic heating, which includes contributions from radiation, sensible heat, and latent heat, is typically estimated using methods described in Li et al. (2023), Ling and Zhang (2013), and Yanai et al. (1973). However, in this study, we focus solely on the anomalous latent heating associated with precipitation anomalies and, therefore, apply the above equation to calculate diabatic heating. The diabatic heating rate was then converted into 20 sigma levels. This vertical heating profile follows a gamma profile (Fig. S2). The maximum thermal forcing, equivalent to H, is set to be at 700 hPa (sigma = 0.8), as the diabatic heating rate typically has maximum at this level during precipitation (Chang and L'Ecuyer 2019; Hagos et al. 2010; Liu et al. 2015). The experiments ran for a total of 28 days, and the results after day 14 were used in this study to exclude the spinup period. The LBM approaches a steady state by day 15 (Watanabe and Jin 2003). Details of the forcing used in the LBM experiments will be given in section 4.

3. Observed interdecadal changes in TCGF and large-scale circulation

Table 1 shows a significant decrease in TCGF over the WNP only in OND in the recent period (1998–2020) compared to the early period (1982–97). In JFM, the mean TCGF increases by 0.3 in the recent period, but this increase is statistically insignificant, as indicated by the p value. The mean TCGF decreases slightly by 0.2 in AMJ, but this change is also statistically insignificant. The TCGF in JAS season decreases by 1.5, a much larger change compared to the previous two seasons, but this change is not significant at a 95% confidence level. This is reasonable given that the change is relatively small compared to the average TCGF in JAS (14.03 TCs during the entire period), which represents the peak TC season. In OND, however, approximately 2.3 fewer TCs formed in the recent period than in the early period. This is about 30% decline in TCGF during this season and is statistically significant at the 95% confidence level.

Seasonal spatial distributions of the interdecadal changes in TCGF and the relative vorticity at 850 hPa are shown in Fig. 3, and the results are consistent with those of Chang et al. (2021). Both TCGF and vorticity show similar patterns over MDRs in all seasons. In contrast to other seasons, abrupt decreases in TCGF and the relative vorticity were observed within the seasonal MDR in OND. However, in JAS, the long-term changes in TCGF and relative vorticity were statistically insignificant, although their spatial patterns show slight similarities to those in OND. This reconfirms that relative vorticity is an important factor controlling TCGF during OND. Note that other variables affecting TC genesis, such as relative humidity at 700 hPa, potential intensity (Bister and Emanuel 2002), and vertical wind shear (VWS) between 200 and 850 hPa, do not clearly match the change over the seasonal MDR (Fig. S3): the relative humidity and the potential intensity increase in all seasons, which is favorable for TC genesis, while the change in the VWS is statistically insignificant over the seasonal MDR. Furthermore, the spatial patterns of the interdecadal changes in TCGF correlate with those of low-level relative vorticity within the WNP, with the weakest correlation in AMJ (r = 0.2) and the strongest in OND (r = 0.32), which are statistically significant at the 99% confidence level (Table S1). The correlations with relative humidity, vertical wind shear, and potential intensity are inconsistent by season and generally produce high p values.

According to Chang et al. (2021), the seasonal differences in the interdecadal changes in precipitation are responsible for the distinct change in the low-level relative vorticity during OND. The most noticeable increases in precipitation are observed over the SCRRs. This can be explained by the rich-get-richer mechanism.

We first reconfirmed the seasonal variation of the SCRRs over the tropics. In Figs. 4a–d, the SCRRs (contours), where the climatological mean precipitation is above 6 mm day^{-1}, are observed in the intertropical convergence zone (ITCZ) and the South Pacific convergence zone (SPCZ), as well as in the tropical Indo-Pacific warm pool region (i.e., 20°S–20°N, 60°E–180°). In particular, the location of the SCRRs exhibits a seasonal cycle in the tropical Indo-Pacific warm pool region: These areas are found in the Indian and western Pacific Oceans during JFM, in the western Pacific during AMJ, further to the northwest during JAS, and back to the west, i.e., the Indian Ocean, during OND. Simultaneously, in the central and eastern Pacific Ocean, the precipitation area in the ITCZ shows a seasonal variation that is analogous to the seasonal cycle found in the tropical Indo-Pacific warm pool.

The precipitation increased overall in the SCRRs across all seasons, as indicated by shadings and contours in Figs. 4a–d. Table 2 presents the specific interdecadal changes in

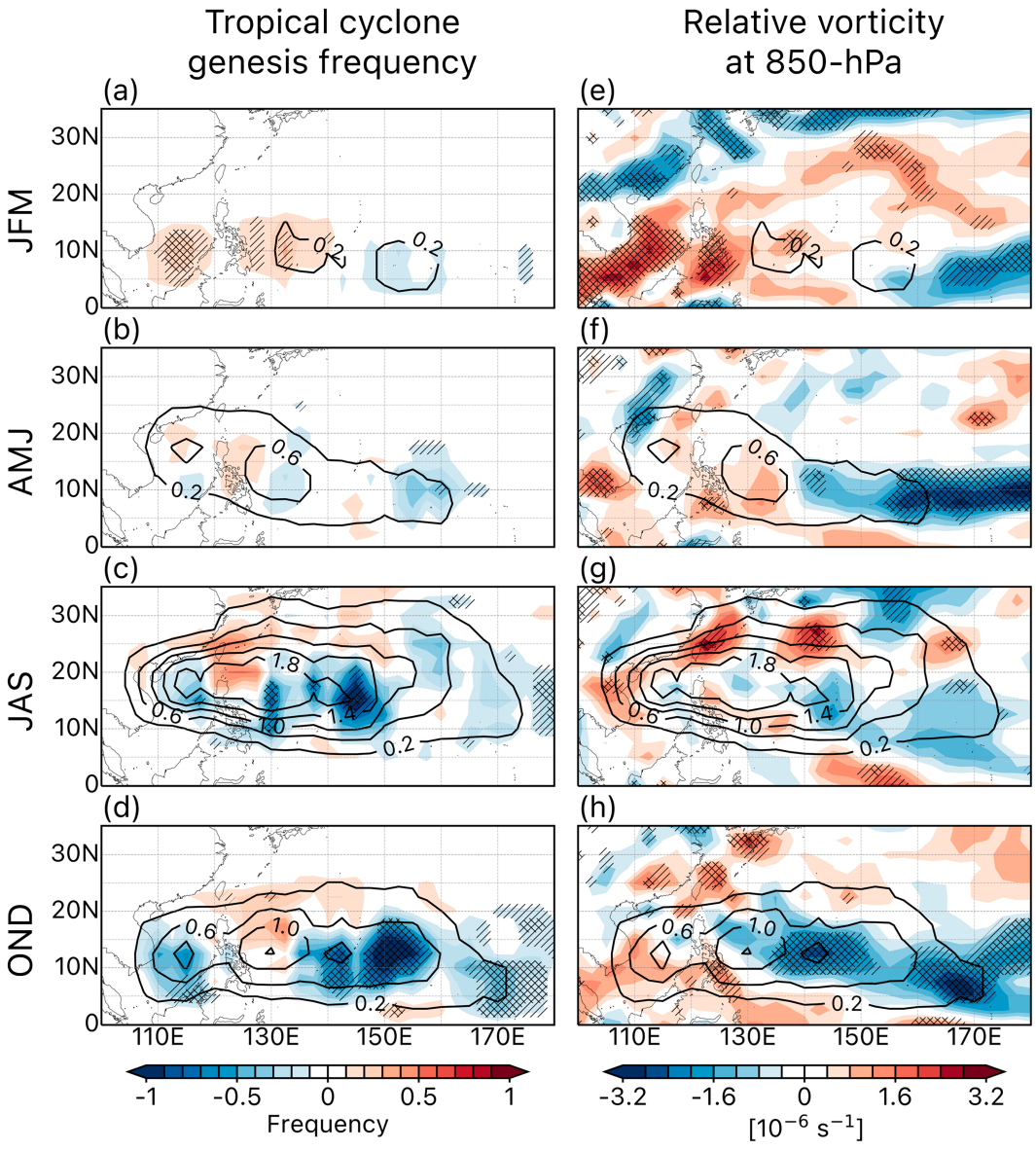

FIG. 3. Horizontal distributions of interdecadal changes in (a)–(d) TCGFs derived from the JTWC best track data and (e)–(h) 850-hPa relative vorticity derived from ERA5 reanalysis data between the early (1982–97) and recent (1998–2020) periods for four seasons. Contours represent the seasonal MDR as the number of TC genesis during the season based on the entire study period. Slashed and crossed areas indicate that the changes are significant at the 90% and 95% confidence levels, respectively.

precipitation (mm day^{-1}) averaged over the areas of the tropical Indian and Pacific Oceans (20°S–20°N, 60°E–90°W), where the climatological precipitation is above or below 6 mm day^{-1}. In the SCRRs, where the climatological precipitation exceeds the threshold, a significant increase in precipitation is observed in AMJ, JAS, and OND. On the other hand, in regions with lower precipitation (i.e., below the threshold), the changes are statistically insignificant, as indicated by the high p value across all seasons. In JFM, the increase in the precipitation within the Indian Ocean is centered north (10°N, 90°–120°E) of the SCRR (south of 0°). This may largely contribute to the low significance of the interdecadal change in the SCRRs in JFM, as shown in Table 2. This could result from mechanisms other than the rich-get-richer mechanism, such as changes in the Hadley circulation. However, confirming this hypothesis requires further investigation, as it is beyond the scope of our study.

The observed increases in precipitation can be attributed to the changes in SSTs. SST has increased within the tropical Indo-Pacific warm pool region, and the horizontal distribution of the increase is similar across seasons (Figs. 4e–h), with correlations between the spatial patterns of all season pairs significant at

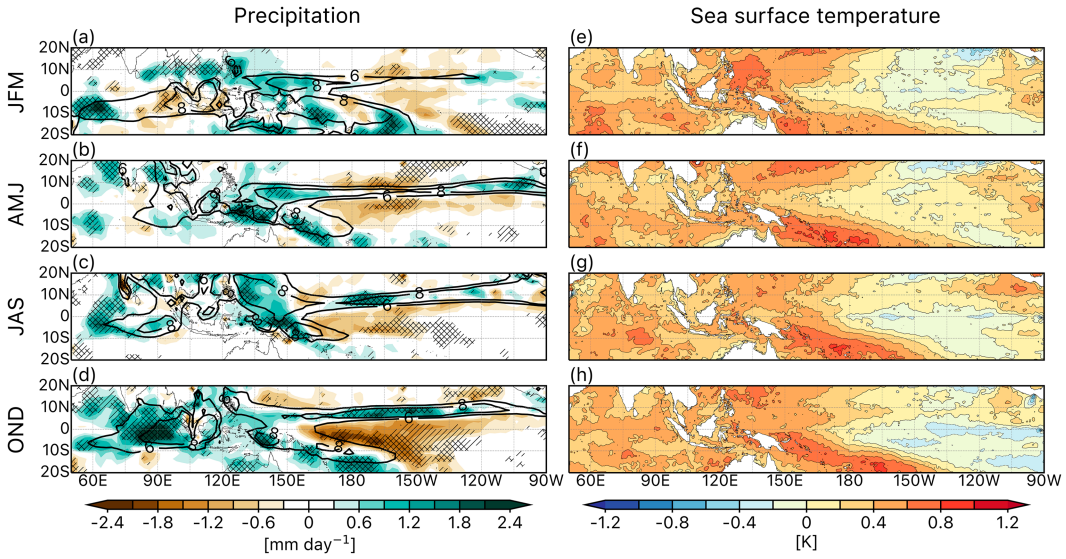

FIG. 4. Spatial distribution of interdecadal changes (shading) in (a)–(d) precipitation and (e)–(h) SST between the early (1982–97) and recent (1998–2020) periods. In (a)–(d), black contours represent seasonal mean precipitation (mm day^{-1}), and slashed and crossed areas indicate that the depicted changes are significant at the 90% and 95% confidence levels, respectively.

the 99% confidence level (not shown). A complex pattern of changes is also found in the tropical eastern Pacific. In the subtropical eastern Pacific, SST cooling is exhibited in both hemispheres, although the cooling signals are relatively weak in the Southern Hemisphere, particularly during JFM and AMJ. In contrast, SST warming is found near the American continent and along the ITCZ. The patterns of the SST changes resemble those of the precipitation changes. Rainfall increases over the SCRRs in the tropical Indo-Pacific warm pool, the SPCZ, and the ITCZ, while rainfall rarely changes or decreases in the other tropical ocean areas.

The observational analysis suggests that the seasonality of the changes in the large-scale circulation can be related to the changes in the precipitation rather than to the changes in the SST. The interdecadal changes in the SST show the La Niña–like pattern across all seasons, which results in the atmospheric boundary layer (ABL) warming and convection strengthening in the SCRRs. According to Chou and Neelin (2004), precipitation tends to increase in the SCRRs under global warming, while it tends to decrease in nonconvective regions. The ABL moisture increases in response to global warming in convective regions, which decreases the gross moist static stability and increases gross moisture stratification (i.e., the direct effect of greater moisture). Chang et al. (2021) suggested that tropical oceanic warming would lead to an increase in low-level moisture, akin to ABL warming under global warming, resulting in enhanced convection over the SCRRs through the rich-get-richer mechanism (Chou and Neelin 2004).

Given the observed data, it seems reasonable to suggest that the seasonality of interdecadal precipitation changes can impact the seasonality of the interdecadal changes in the large-scale circulation over the WNP. To further examine this relationship, we employed numerical model simulations. Additionally, we aimed to determine whether the precipitation changes over the Indo-Pacific warm pool alone can drive the observed changes in the large-scale circulation in the WNP, as suggested by Chang et al. (2021), or if changes in other basins also influence the large-scale circulation in the WNP.

TABLE 2. Interdecadal differences in precipitation (mm day^{-1}) between the early (1982–97) and recent (1998–2020) periods in the regions where the climatological precipitation is either above or below the threshold value of 6 mm day^{-1} in the tropical Indian and Pacific Oceans (20°S–20°N, 60°E–90°W). Values in parentheses indicate the p value of the interdecadal differences.

	Above 6 mm day^{-1}	Below 6 mm day^{-1}
JFM	+0.274 (0.15)	−0.021 (0.83)
AMJ	+0.393 (0.02)	−0.049 (0.47)
JAS	+0.329 (0.01)	−0.067 (0.34)
OND	+0.602 (<0.01)	−0.133 (0.08)

4. Simulated changes in precipitation and large-scale circulation

Two simulations were conducted using MPAS-A. In the CTRL simulation, we prescribed the daily climatological mean SST from 1982 to 2020 for the entire simulation period. The experimental simulation, identified as L-WARM, was designed to incorporate interdecadal SST changes, specifically the La Niña–like SST pattern. For the L-WARM simulation, we added the daily SST anomalies over the tropics (20°S–20°N) to the climatological SST used in the CTRL simulation. To reduce model instability caused by drastic changes in the SST at the boundaries (i.e., 20°S and 20°N), we applied a buffer zone of 10° toward higher latitudes (Fig. 5). The L-WARM simulation was

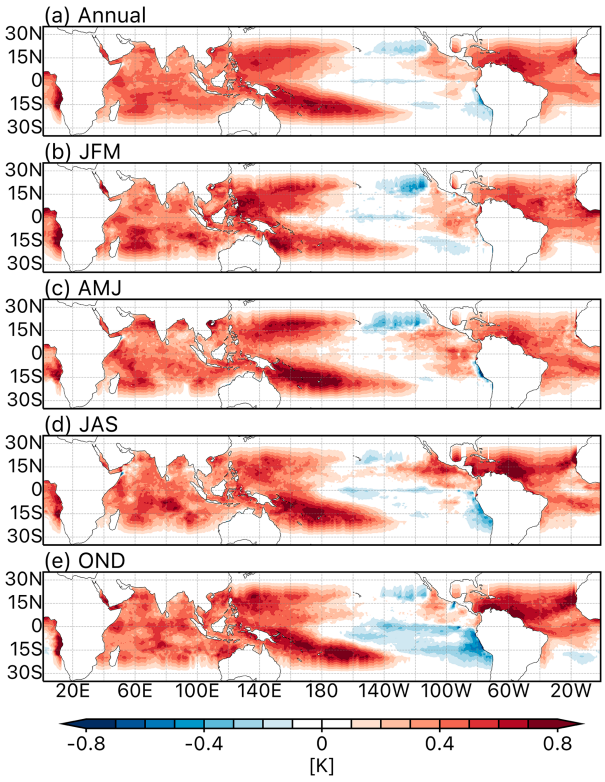

FIG. 5. Interdecadal changes of annual and seasonal SST—(a) January–December, (b) JFM, (c) AMJ, (d) JAS, and (e) OND. All of them were used as forcing for MPAS-A experiments.

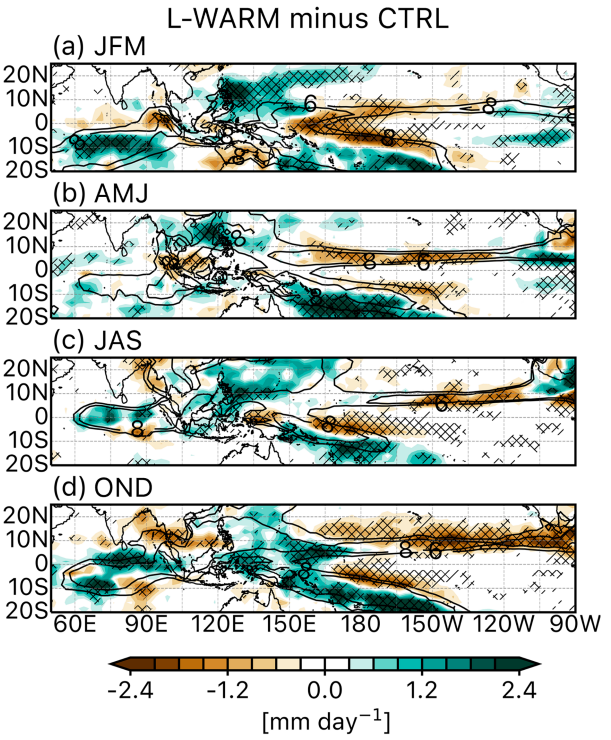

FIG. 6. Seasonal-mean precipitation of the CTRL simulation (contours) and the changes in the simulated precipitation of the L-WARM relative to that of CTRL (shadings) over four seasons: (a) JFM, (b) AMJ, (c) JAM, and (d) OND. Slashed and crossed areas indicate that the depicted changes are significant at 90% and 95% confidence levels, respectively.

implemented to examine whether MPAS-A can simulate the observed precipitation changes under conditions reflecting the La Niña–like SST warming pattern.

According to the results, the rich-get-richer mechanism seems to explain the increased precipitation within the Indo-Pacific warm pool region under La Niña–like SST warming. Figure 6 shows the seasonal averages of the CTRL simulation (contours) and the changes in the simulated precipitation of the L-WARM relative to that of the CTRL (shadings). The seasonal cycle of precipitation patterns simulated in the CTRL is comparable to the observed precipitation (Figs. 4a–d and 6a–d), although the simulated precipitation is overestimated overall. In terms of the location of the SCRRs, this seasonal cycle pattern is maintained in the L-WARM (Fig. S4), but there is stronger precipitation over the SCRRs under La Niña–like SST warming compared to the CTRL (Fig. 6) over the Indo-Pacific warm pool region, where the increases in SSTs were more pronounced. These results confirm that the rich-get-richer mechanism is valid in the tropical Indo-Pacific warm pool region under La Niña–like SST changes. As in the observed precipitation patterns, in JFM, the L-WARM simulation produced a precipitation decrease within the SCRR in the eastern Indian Ocean, which again suggests that another mechanism may be at work in JFM. In summary, based on the MPAS-A simulation, the precipitation tends to increase over the SCRRs in the Indo-Pacific warm pool region in response to La Niña–like SST warming, which implies that the rich-get-richer mechanism is valid.

On the other hand, simulated precipitation decreases in the equatorial convergence zone of the central and eastern Pacific Ocean (i.e., 180°–100°W), which contrasts with the observed changes in precipitation, especially in JAS and OND (Figs. 4c,d and 6c,d). These discrepancies can be attributed to the inherent limitations of the model. The observed increases in precipitation are likely associated with a local response to the zonal SST ridge in the ITCZ depicted in Figs. 4g and 4h. However, in the model simulation, the strong zonal gradient in SSTs that characterizes the La Niña–like SST pattern is likely to be a dominant factor, leading to an intensification of the Walker circulation and a reduction in rainfall over the equatorial central and eastern Pacific Ocean.

The differences in the simulated relative vorticity and horizontal winds at 850 hPa between the L-WARM and CTRL simulations are shown in Fig. 7. In JFM and AMJ (Figs. 7a,b), there are minor changes in the large-scale flow over the seasonal MDRs (contours), with patterns comparable to those in the observed data (Figs. 3e,f). In JAS, there is an anomalous cyclonic flow across the MDR, which would be favorable for TC development. The changes in the 850-hPa relative vorticity patterns in the L-WARM relative to the CTRL generally resemble the observed interdecadal changes in JFM, AMJ, and JAS

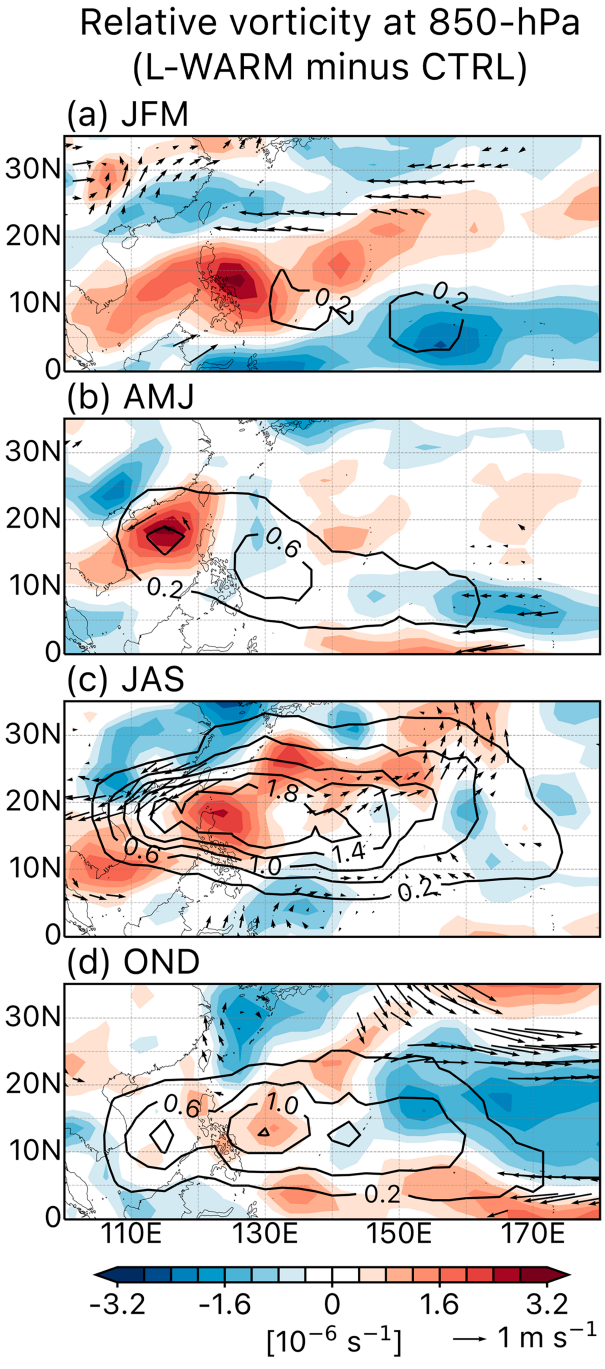

FIG. 7. Changes in relative vorticity (10^{-6} s^{-1}; shadings) and horizontal winds at 850 hPa (m s^{-1}; vectors) in the L-WARM relative to the CTRL, both based on MPAS-A, over four seasons: (a) JFM, (b) AMJ, (c) JAS, and (d) OND. Vectors are plotted where the changes in wind are statistically significant at the 95% confidence level. Black contours indicate the seasonal MDRs based on the JTWC best track data, which are as in Fig. 1.

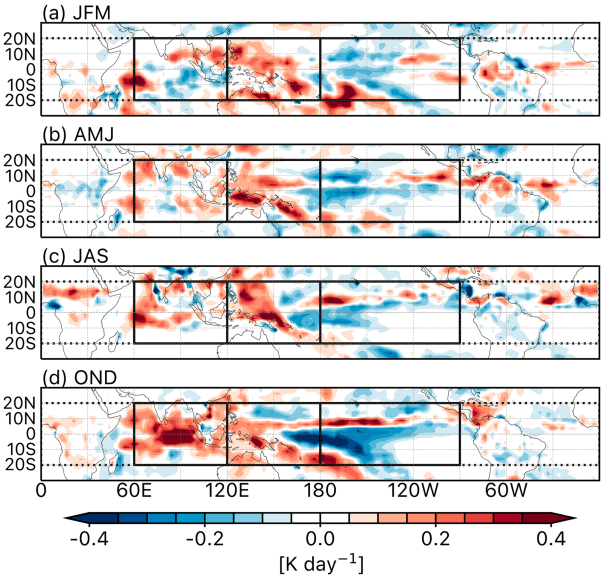

FIG. 8. Diabatic heating rates during (a) JFM, (b) AMJ, (c) JAS, and (d) OND. These patterns are calculated from observed precipitation anomalies and are applied to the LBM experiments. Solid-boxed and dotted regions represent the areas in which the forcing is prescribed in each experiment. These include the tropical Indian Ocean (20°S–20°N, 60°–120°E), the Indo-Pacific warm pool (20°S–20°N, 60°E–180°), the tropical Indian and Pacific Oceans (20°S–20°N, 60°E–90°W), and the tropical band (20°S–20°N), respectively.

seasons. Notably, the patterns are inconsistent and insignificant over the MDR, although some discrepancies remain. In particular, the positive anomalies are stronger, and the negative anomalies are weaker than observed changes in JAS season. On the other hand, in OND, a weak anomalous anticyclone is present, confined to the east of the seasonal MDR, which differs somewhat from the observed patterns. This discrepancy is discussed more in section 5. Additionally, whereas the patterns in JAS and OND show similarities in observations (Figs. 3g,h), they are not well captured in the model results. Moreover, the pattern correlation between observations and simulations is relatively high during JFM (0.6406) and AMJ (0.5035) but drops significantly during JAS (0.002) and OND (0.1654). This suggests that MPAS-A struggles to reproduce accurately the atmospheric circulation patterns in these seasons. These results indicate a seasonal dependence in the MPAS-A simulation, with better performance in capturing large-scale circulation changes in JFM and AMJ compared to JAS and OND.

Experimental simulations based on the LBM were conducted to determine whether the changes in precipitation directly cause the changes in large-scale circulation over the seasonal MDRs in the WNP. This model was used instead of MPAS-A due to the limitations of MPAS-A simulations discussed above. Moreover, the LBM experiments were implemented to examine whether precipitation changes in other basins can affect the large-scale circulation over the WNP. Four LBM simulations were conducted for each season (JFM, AMJ, JAS, and OND). The experiments were conducted in response to the diabatic heating rates calculated based on the observed precipitation anomalies in the tropical Indian Ocean (20°S–20°N, 60°–120°E), the Indo-Pacific warm pool (20°S–20°N, 60°E–180°), both the

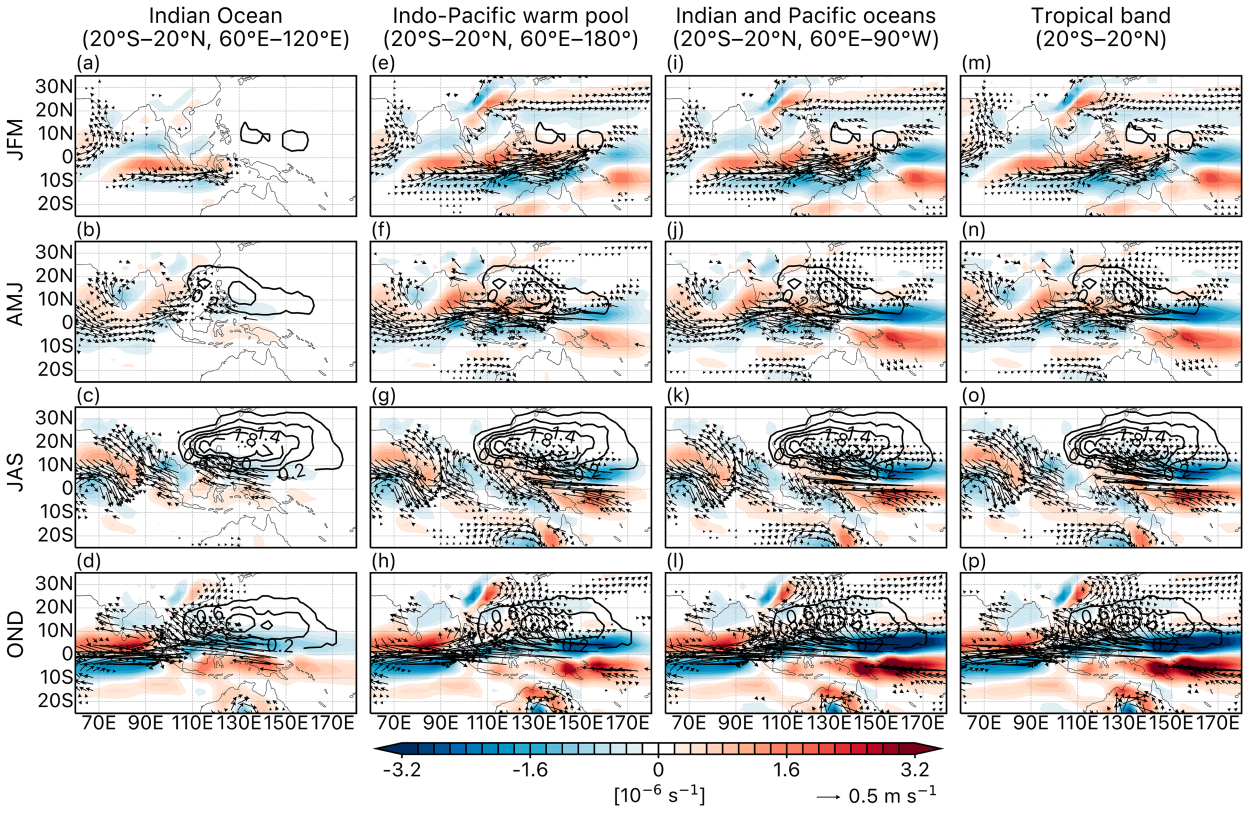

FIG. 9. Horizontal distributions of the seasonal anomalies in relative vorticity (shadings) and horizontal winds (vectors) at 850 hPa simulated by LBM. The results of four experiments, which were, respectively, forced by diabatic heating rates calculated from the observed changes in precipitation over (first column) the tropical Indian Ocean (20°S–20°N, 60°–120°E), (second column) the Indo-Pacific warm pool (20°S–20°N, 60°E–180°), (third column) the tropical Indian and Pacific Oceans (20°S–20°N, 60°E–90°W), and (fourth column) the tropical band (20°S–20°N), are presented for four seasons: (first row) JFM, (second row) AMJ, (third row) JAS, and (fourth row) OND. Vectors are plotted at the points where the average wind speed is 0.5 m s^{-1} or greater. Black contours indicate the seasonal MDRs based on the JTWC best track data, which are as in Fig. 1.

tropical Indian Ocean and tropical Pacific Ocean (20°S–20°N, 60°E–90°W), and the tropical band (20°S–20°N), respectively. The spatial distributions of the seasonal diabatic heating rates are identical to those of the observed seasonal anomalies of the precipitation. In OND, the strong diabatic heating is observed in the tropical Indian Ocean, while it is located around the Maritime Continent and in the western Pacific in JFM, AMJ, and JAS (Fig. 8).

Figure 9 shows the spatial distributions of the relative vorticity and the horizontal wind at 850 hPa over the WNP, as simulated by the LBM experiments. In all four simulations, pronounced anomalous easterlies and anticyclonic flow are observed over the WNP during OND, which is distinct from other seasons. However, when the thermal forcing is applied only over the Indian Ocean (20°S–20°N, 60°–120°E) or the Indo-Pacific warm pool (20°S–20°N, 60°E–180°), the wind anomalies are much weaker than in simulations where diabatic heating is imposed over both the Indian and Pacific Oceans (20°S–20°N, 60°E–90°W) or across the entire tropical band. In the latter cases, the induced easterlies and the anticyclones become stronger and extend westward in OND season (Figs. 9i–p), suggesting that the precipitation changes in the Indian and Pacific Oceans contribute to modulating large-scale circulation over the WNP.

This conclusion is further supported by the pattern correlation between ERA5 and the tropical band experiment using LBM (Figs. 9m–p). The correlation coefficients in the seasonal MDR were 0.3967 (JFM), 0.2456 (AMJ), 0.2769 (JAS), and 0.2259 (OND), all statistically significant at the 99% confidence level. These results suggest that precipitation anomalies over the Indian and Pacific Oceans influence atmospheric circulation over the WNP. Thus, the weaker and smaller anomalous anticyclones during OND in the MPAS-A simulation compared to observations (Figs. 3h and 7d) are likely due to MPAS-A's inability to accurately simulate precipitation patterns, which in turn limits its ability to capture the associated atmospheric circulation over the WNP.

5. Summary and discussion

This study aims to validate the mechanism driving the decline in TCGF over the WNP seen in recent decades through a series of model experiments. Previously, Chang et al. (2021) highlighted this phenomenon, suggesting a link between the

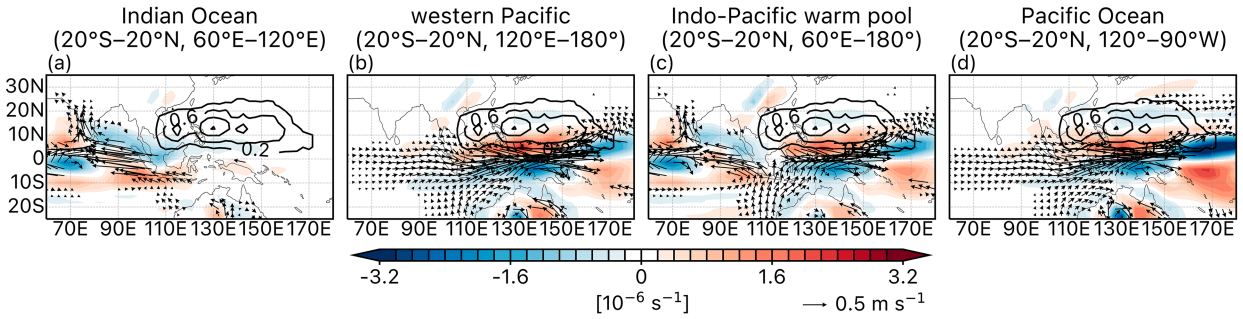

FIG. 10. Horizontal distributions of the anomalies of relative vorticity (shadings) and horizontal wind (vectors) at 850 hPa in OND, which are simulated from the LBM experiments. The experiments were forced by diabatic heating rate calculated from the simulated changes in precipitation over (a) the tropical Indian Ocean (20°S–20°N, 60°–120°E), (b) the western Pacific (20°S–20°N, 120°E–180°), (c) Indo-Pacific warm pool (20°S–20°N, 60°E–180°), and the Pacific Ocean (20°S–20°N, 120°E–90°W) and are represented. Vectors are plotted at the points where the wind speed is 0.5 m s^{-1} or greater. Black contours indicate the seasonal MDR region based on the JTWC best track data, which is as in Fig. 1.

seasonal changes in precipitation and those in large-scale anticyclones in the MDRs, thereby influencing the TCGF. However, the underlying mechanism remained unverified due to a reliance on observational analysis alone.

To address this gap, this study conducted model experiments using MPAS-A and LBM. First, two experiments were conducted using MPAS-A: CTRL and the L-WARM. These experiments were implemented in response to the daily SST climatology and the climatology plus La Niña–like SST changes, respectively. In the L-WARM scenario, the precipitation increased, particularly in the SCRRs within the Indo-Pacific warm pool region. Subsequently, the LBM experiments were conducted to examine the direct influence of observed increases in precipitation on large-scale circulation in the WNP, prescribing thermal forcing based on the seasonal precipitation changes. The results showed that when the changes in precipitation in both the tropical Indian Ocean and the tropical Pacific Ocean are considered collectively, the anomalous anticyclonic flow is more intense and extends further westward in OND than in other seasons over the WNP.

Thus, the series of model experiments implemented in this study provided evidence that validated two hypotheses: Based on the MPAS-A experiments, the observed La Niña–like SST warming was found to be responsible for the precipitation increases in the SCRRs of the Indo-Pacific warm pool. The LBM experiments revealed that the changes in precipitation in both the Indo-Pacific warm pool and the eastern Pacific played an instrumental role in influencing the changes in the large-scale circulation over the WNP. The first conclusion verifies the concept introduced by Chang et al. (2021), and the second adds a new dimension, as the previous study solely focused on the precipitation increases in the Indo-Pacific warm pool region.

The MPAS-A shows some limitations in simulating changes in precipitation under La Niña–like SST warming. Compared to the observed changes in precipitation, the model simulation could not capture increases in precipitation in the ITCZ, especially in JAS and OND. This suggests that the MPAS-A failed to simulate the local responses of precipitation to the warm SST ridge in the ITCZ. The lower-tropospheric relative vorticity exhibited a pattern comparable to that of the observations over the MDRs from January to September, whereas in OND, the anomalous anticyclone is confined more to the eastern WNP compared to the observation. This discrepancy between the observed and the simulated large-scale circulations in OND (cf. Figs. 3h and 7d) can be attributed to a competition between two enhanced precipitations, one in the 70°–90°E region and the other in the 150°–170°E region of the model results (Fig. 6d). The observed increase in precipitation in the Indian Ocean is prevailing within the Indo-Pacific warm pool region (Fig. 4d), resulting in the anomalous easterlies extending further westward (Fig. 3h). On the other hand, in the result of MPAS-A simulation, the precipitation increases over both the western Pacific and the Indian Oceans, which hinders the strengthening and westward extension of the anomalous easterlies. This argument is supported by the LBM experiments, which are forced by the simulated precipitation changes only over the warm pool region (Figs. 9h and 10a–c). Furthermore, based on the LBM experiments forced by simulated precipitation anomalies, the discrepancies between the simulated and observed precipitation changes over the ITCZ in the central to eastern Pacific—where the simulations show a decrease while the observations indicate an increase—may contribute to the differences in the simulated large-scale circulation compared to observation. The LBM experiments suggest that the reduced precipitation over the central to eastern Pacific may strengthen the easterly anomalies over the tropics in the southeast of the WNP (Figs. 10b,d). However, this effect is unlikely to cause a significant difference between the observed and simulated large-scale circulation.

A limitation of our model configuration is that TC genesis was not captured directly due to the low model resolution of 240 km. Many studies have shown that horizontal resolution influences the simulation of TC information, such as formation, intensity, and track, considerably (Roberts et al. 2020; Walsh et al. 2013; Wehner et al. 2014; Zhao et al. 2009). Our model results indicate that the observed changes in the large-scale environmental factors that can affect TC genesis can

largely be simulated using numerical models. Although large-scale circulation, including low-level relative vorticity, affects TC genesis, our results could not show that the simulated differences in the large-scale circulation between the L-WARM and CTRL simulations influenced TC genesis directly. In future research, it would be meaningful to investigate how well TCs can be simulated using the MPAS-A at a resolution higher than 25 km.

Acknowledgments. This study was supported by the National Research Foundation of the Korean government (RS-2023-00207866) and the Korea Meteorological Administration Research and Development Program (RS-2022-KM221312). We have no conflicts of interest.

Data availability statement. The best track datasets are available for download via JTWC (https://www.metoc.navy.mil/jtwc/jtwc.html?best-tracks) and RSMC (https://www.jma.go.jp/jma/jma-eng/jma-center/rsmc-hp-pub-eg/besttrack.html). The OISST and GPCP datasets are available for download via the Physical Sciences Laboratory (https://psl.noaa.gov/data/gridded/data.noaa.oisst.v2.highres.html and https://psl.noaa.gov/data/gridded/data.gpcp.html, respectively). The ERA5 reanalysis datasets are available for download via the Copernicus Climate Data Store (https://cds.climate.copernicus.eu/datasets/reanalysis-era5-pressure-levels-monthly-means?tab=overview and https://cds.climate.copernicus.eu/datasets/reanalysis-era5-pressure-levels?tab=overview).

REFERENCES

Adler, R. F., and Coauthors, 2018: The Global Precipitation Climatology Project (GPCP) monthly analysis (new version 2.3) and a review of 2017 global precipitation. *Atmosphere*, **9**, 138, https://doi.org/10.3390/atmos9040138.

An, S.-I., J.-W. Kim, S.-H. Im, B.-M. Kim, and J.-H. Park, 2012: Recent and future sea surface temperature trends in tropical Pacific warm pool and cold tongue regions. *Climate Dyn.*, **39**, 1373–1383, https://doi.org/10.1007/s00382-011-1129-7.

Annamalai, H., 2010: Moist dynamical linkage between the equatorial Indian Ocean and the South Asian monsoon trough. *J. Atmos. Sci.*, **67**, 589–610, https://doi.org/10.1175/2009JAS2991.1.

Baik, J.-J., and J.-S. Paek, 2001: Relationship between vertical wind shear and typhoon intensity change, and development of three-predictor intensity prediction model. *J. Meteor. Soc. Japan*, **79**, 695–700, https://doi.org/10.2151/jmsj.79.695.

Bister, M., and K. A. Emanuel, 2002: Low frequency variability of tropical cyclone potential intensity 1. Interannual to interdecadal variability. *J-Geophys-Res.*, **107**, https://doi.org/10.1029/2001JD000776.

Cao, X., S. Chen, G. Chen, and R. Wu, 2016: Intensified impact of northern tropical Atlantic SST on tropical cyclogenesis frequency over the western North Pacific after the late 1980s. *Adv. Atmos. Sci.*, **33**, 919–930, https://doi.org/10.1007/s00376-016-5206-z.

Chang, K.-W., and T. S. L'Ecuyer, 2019: Role of latent heating vertical distribution in the formation of the tropical cold trap. *J. Geophys. Res. Atmos.*, **124**, 7836–7851, https://doi.org/10.1029/2018JD030194.

Chang, M., D.-S. R. Park, and C.-H. Ho, 2021: Possible cause of seasonal inhomogeneity in interdecadal changes of tropical cyclone genesis frequency over the western North Pacific. *J. Climate*, **34**, 635–642, https://doi.org/10.1175/JCLI-D-20-0268.1.

Choi, Y., K.-J. Ha, C.-H. Ho, and C. E. Chung, 2015: Interdecadal change in typhoon genesis condition over the western North Pacific. *Climate Dyn.*, **45**, 3243–3255, https://doi.org/10.1007/s00382-015-2536-y.

Chou, C., and J. D. Neelin, 2004: Mechanisms of global warming impacts on regional tropical precipitation. *J. Climate*, **17**, 2688–2701, https://doi.org/10.1175/1520-0442(2004)017<2688:MOGWIO>2.0.CO;2.

Deng, L., Y. Zhao, W. Gao, L. Xue, and Y. Duan, 2021: Intensity and microphysical properties surrounding the rapid intensification in landfalling Super Typhoons over China during the summer and autumn seasons. *Intl. J. Climatol.*, **41**, 6366–6381, https://doi.org/10.1002/joc.7200.

Gray, W. M., 1968: Global view of the origin of tropical disturbances and storms. *Mon. Wea. Rev.*, **96**, 669–700, https://doi.org/10.1175/1520-0493(1968)096<0669:GVOTOO>2.0.CO;2.

Grell, G. A., and S. R. Freitas, 2014: A scale and aerosol aware stochastic convective parameterization for weather and air quality modeling. *Atmos. Chem. Phys.*, **14**, 5233–5250, https://doi.org/10.5194/acp-14-5233-2014.

Guo, Y.-P., X. Feng, N. P. Klingaman, and Z.-M. Tan, 2020: Impact of Indo-Pacific warm pool Hadley circulation on the seasonal forecast performance for summer precipitation over the western North Pacific. *Environ. Res. Lett.*, **15**, 104041, https://doi.org/10.1088/1748-9326/aba97c.

Hagos, S., and Coauthors, 2010: Estimates of tropical diabatic heating profiles: Commonalities and uncertainties. *J. Climate*, **23**, 542–558, https://doi.org/10.1175/2009JCLI3025.1.

Han, W., G. A. Meehl, A. Hu, J. Zheng, J. Kenigson, J. Vialard, and B. Rajagopalan, Yanto, 2017: Decadal variability of the Indian and Pacific Walker cells since the 1960s: Do they covary on decadal time scales? *J. Climate*, **30**, 8447–8468, https://doi.org/10.1175/JCLI-D-16-0783.1.

He, H., J. Yang, D. Gong, R. Mao, Y. Wang, and M. Gao, 2015: Decadal changes in tropical cyclone activity over the western North Pacific in the late 1990s. *Climate Dyn.*, **45**, 3317–3329, https://doi.org/10.1007/s00382-015-2541-1.

Hersbach, H., and Coauthors, 2020: The ERA5 global reanalysis. *Quart. J. Roy. Meteor. Soc.*, **146**, 1999–2049, https://doi.org/10.1002/qj.3803.

Holton, J. R., and G. J. Hakim, 2013: Tropical dynamics. *An Introduction to Dynamic Meteorology*, 5th ed. J. R. Holton and G. J. Hakim, Eds., Academic Press, 377–411.

Hong, C.-C., Y.-K. Wu, T. Li, and C.-C. Chang, 2014: The climate regime shift over the Pacific during 1996/1997. *Climate Dyn.*, **43**, 435–446, https://doi.org/10.1007/s00382-013-1867-9.

——, ——, and ——, 2016: Influence of climate regime shift on the interdecadal change in tropical cyclone activity over the Pacific Basin during the middle to late 1990s. *Climate Dyn.*, **47**, 2587–2600, https://doi.org/10.1007/s00382-016-2986-x.

Hong, S.-Y., and J.-O. J. Lim, 2006: The WRF Single-Moment 6-class Microphysics scheme (WSM6). *Asia-Pac. J. Atmos. Sci.*, **42**, 129–151.

Hsu, P.-C., P.-S. Chu, H. Murakami, and X. Zhao, 2014: An abrupt decrease in the late-season typhoon activity over the western North Pacific. *J. Climate*, **27**, 4296–4312, https://doi.org/10.1175/JCLI-D-13-00417.1.

Hu, J., and A. Duan, 2015: Relative contributions of the Tibetan Plateau thermal forcing and the Indian Ocean sea surface temperature basin mode to the interannual variability of the East Asian summer monsoon. *Climate Dyn.*, **45**, 2697–2711, https://doi.org/10.1007/s00382-015-2503-7.

Huang, P., C. Chou, and R. Huang, 2011: Seasonal modulation of tropical intraseasonal oscillations on tropical cyclone geneses in the western North Pacific. *J. Climate*, **24**, 6339–6352, https://doi.org/10.1175/2011JCLI4200.1.

Huangfu, J., R. Huang, and W. Chen, 2018: Interdecadal variation of tropical cyclone genesis and its relationship to the convective activities over the central Pacific. *Climate Dyn.*, **50**, 1439–1450, https://doi.org/10.1007/s00382-017-3697-7.

Huo, L., P. Guo, S. N. Hameed, and D. Jin, 2015: The role of tropical Atlantic SST anomalies in modulating western North Pacific tropical cyclone genesis. *Geophys. Res. Lett.*, **42**, 2378–2384, https://doi.org/10.1002/2015GL063184.

Jin, F.-F., L.-L. Pan, and M. Watanabe, 2006: Dynamics of synoptic eddy and low-frequency flow interaction. Part I: A linear closure. *J. Atmos. Sci.*, **63**, 1677–1694, https://doi.org/10.1175/JAS3715.1.

Karnauskas, K. B., R. Seager, A. Kaplan, Y. Kushnir, and M. A. Cane, 2009: Observed strengthening of the zonal sea surface temperature gradient across the equatorial Pacific Ocean. *J. Climate*, **22**, 4316–4321, https://doi.org/10.1175/2009JCLI2936.1.

Kim, J.-H., C.-H. Ho, and P.-S. Chu, 2010: Dipolar redistribution of summertime tropical cyclone genesis between the Philippine Sea and the northern South China Sea and its possible mechanisms. *J. Geophys. Res.*, **115**, D06104, https://doi.org/10.1029/2009JD012196.

Klemp, J. B., 2011: A terrain-following coordinate with smoothed coordinate surfaces. *Mon. Wea. Rev.*, **139**, 2163–2169, https://doi.org/10.1175/MWR-D-10-05046.1.

Kohyama, T., D. L. Hartmann, and D. S. Battisti, 2017: La Niña–like mean-state response to global warming and potential oceanic roles. *J. Climate*, **30**, 4207–4225, https://doi.org/10.1175/JCLI-D-16-0441.1.

Kosaka, Y., and S.-P. Xie, 2013: Recent global-warming hiatus tied to equatorial Pacific surface cooling. *Nature*, **501**, 403–407, https://doi.org/10.1038/nature12534.

——, H. Nakamura, M. Watanabe, and M. Kimoto, 2009: Analysis on the dynamics of a wave-like teleconnection pattern along the summertime Asian jet based on a reanalysis dataset and climate model simulations. *J. Meteor. Soc. Japan*, **87**, 561–580, https://doi.org/10.2151/jmsj.87.561.

Kossin, J. P., K. R. Knapp, D. J. Vimont, R. J. Murnane, and B. A. Harper, 2007: A globally consistent reanalysis of hurricane variability and trends. *Geophys. Res. Lett.*, **34**, L04815, https://doi.org/10.1029/2006GL028836.

Li, S., T. Sato, T. Nakamura, and W. Guo, 2023: East Asian summer rainfall stimulated by subseasonal Indian monsoonal heating. *Nat. Commun.*, **14**, 5932, https://doi.org/10.1038/s41467-023-41644-5.

Lian, T., D. Chen, J. Ying, P. Huang, and Y. Tang, 2018: Tropical Pacific trends under global warming: El Niño-like or La Niña-like? *Natl. Sci. Rev.*, **5**, 810–812, https://doi.org/10.1093/nsr/nwy134.

Ling, J., and C. Zhang, 2013: Diabatic heating profiles in recent global reanalyses. *J. Climate*, **26**, 3307–3325, https://doi.org/10.1175/JCLI-D-12-00384.1.

Liu, C., S. Shige, Y. N. Takayabu, and E. Zipser, 2015: Latent heating contribution from precipitation systems with different sizes, depths, and intensities in the tropics. *J. Climate*, **28**, 186–203, https://doi.org/10.1175/JCLI-D-14-00370.1.

——, W. Zhang, X. Geng, M. F. Stuecker, and F.-F. Jin, 2019: Modulation of tropical cyclones in the southeastern part of western North Pacific by tropical Pacific decadal variability. *Climate Dyn.*, **53**, 4475–4488, https://doi.org/10.1007/s00382-019-04799-w.

Liu, K. S., and J. C. L. Chan, 2013: Inactive period of western North Pacific tropical cyclone activity in 1998–2011. *J. Climate*, **26**, 2614–2630, https://doi.org/10.1175/JCLI-D-12-00053.1.

Lu, R., and Z. Lin, 2009: Role of subtropical precipitation anomalies in maintaining the summertime meridional teleconnection over the western North Pacific and East Asia. *J. Climate*, **22**, 2058–2072, https://doi.org/10.1175/2008JCLI2444.1.

McPhaden, M. J., T. Lee, and D. McClurg, 2011: El Niño and its relationship to changing background conditions in the tropical Pacific Ocean. *Geophys. Res. Lett.*, **38**, L15709, https://doi.org/10.1029/2011GL048275.

Murakami, H., and B. Wang, 2010: Future change of North Atlantic tropical cyclone tracks: Projection by a 20-km-mesh global atmospheric model. *J. Climate*, **23**, 2699–2721, https://doi.org/10.1175/2010JCLI3338.1.

Nakanishi, M., and H. Niino, 2009: Development of an improved turbulence closure model for the atmospheric boundary layer. *J. Meteor. Soc. Japan*, **87**, 895–912, https://doi.org/10.2151/jmsj.87.895.

Niu, G.-Y., and Coauthors, 2011: The community Noah land surface model with multiparameterization options (Noah-MP): 1. Model description and evaluation with local-scale measurements. *J. Geophys. Res.*, **116**, D12109, https://doi.org/10.1029/2010JD015139.

Park, D.-S. R., C.-H. Ho, J.-H. Kim, and H.-S. Kim, 2011: Strong landfall typhoons in Korea and Japan in a recent decade. *J. Geophys. Res.*, **116**, D07105, https://doi.org/10.1029/2010JD014801.

——, ——, ——, and ——, 2013: Spatially inhomogeneous trends of tropical cyclone intensity over the western North Pacific for 1977–2010. *J. Climate*, **26**, 5088–5101, https://doi.org/10.1175/JCLI-D-12-00386.1.

——, ——, J. C. L. Chan, K.-J. Ha, H.-S. Kim, J. Kim, and J.-H. Kim, 2017: Asymmetric response of tropical cyclone activity to global warming over the North Atlantic and western North Pacific from CMIP5 model projections. *Sci. Rep.*, **7**, 41354, https://doi.org/10.1038/srep41354.

Reynolds, R. W., T. M. Smith, C. Liu, D. B. Chelton, K. S. Casey, and M. G. Schlax, 2007: Daily high-resolution-blended analyses for sea surface temperature. *J. Climate*, **20**, 5473–5496, https://doi.org/10.1175/2007JCLI1824.1.

Ringler, T., L. Ju, and M. Gunzburger, 2008: A multiresolution method for climate system modeling: Application of spherical centroidal Voronoi tessellations. *Ocean Dyn.*, **58**, 475–498, https://doi.org/10.1007/s10236-008-0157-2.

Ringler, T. D., J. Thuburn, J. B. Klemp, and W. C. Skamarock, 2010: A unified approach to energy conservation and potential vorticity dynamics for arbitrarily-structured C-grids. *J. Comput. Phys.*, **229**, 3065–3090, https://doi.org/10.1016/j.jcp.2009.12.007.

Roberts, M. J., and Coauthors, 2020: Impact of model resolution on tropical cyclone simulation using the HighResMIP–PRIMAVERA multimodel ensemble. *J. Climate*, **33**, 2557–2583, https://doi.org/10.1175/JCLI-D-19-0639.1.

Shan, K., and X. Yu, 2020: Interdecadal variability of tropical cyclone genesis frequency in western North Pacific and South

Pacific Ocean basins. *Environ. Res. Lett.*, **15**, 064030, https://doi.org/10.1088/1748-9326/ab8093.

Sharmila, S., and K. J. E. Walsh, 2017: Impact of large-scale dynamic versus thermodynamic climate conditions on contrasting tropical cyclone genesis frequency. *J. Climate*, **30**, 8865–8883, https://doi.org/10.1175/JCLI-D-16-0900.1.

Shin, H. H., S.-Y. Hong, J. Dudhia, and Y.-J. Kim, 2010: Orography-induced gravity wave drag parameterization in the global WRF: Implementation and sensitivity to shortwave radiation schemes. *Adv. Meteor.*, **2010**, 959014, https://doi.org/10.1155/2010/959014.

Skamarock, W. C., J. B. Klemp, M. G. Duda, L. D. Fowler, S.-H. Park, and T. D. Ringler, 2012: A multiscale nonhydrostatic atmospheric model using centroidal Voronoi tesselations and C-grid staggering. *Mon. Wea. Rev.*, **140**, 3090–3105, https://doi.org/10.1175/MWR-D-11-00215.1.

Sohn, B. J., S.-W. Yeh, J. Schmetz, and H.-J. Song, 2013: Observational evidences of Walker circulation change over the last 30 years contrasting with GCM results. *Climate Dyn.*, **40**, 1721–1732, https://doi.org/10.1007/s00382-012-1484-z.

Walsh, K., S. Lavender, E. Scoccimarro, and H. Murakami, 2013: Resolution dependence of tropical cyclone formation in CMIP3 and finer resolution models. *Climate Dyn.*, **40**, 585–599, https://doi.org/10.1007/s00382-012-1298-z.

Watanabe, M., and M. Kimoto, 2000: Atmosphere-ocean thermal coupling in the North Atlantic: A positive feedback. *Quart. J. Roy. Meteor. Soc.*, **126**, 3343–3369, https://doi.org/10.1256/smsqj.57016.

——, and F.-F. Jin, 2003: A moist linear baroclinic model: Coupled dynamical–convective response to El Niño. *J. Climate*, **16**, 1121–1139, https://doi.org/10.1175/1520-0442(2003)16<1121:AMLBMC>2.0.CO;2.

Wehner, M. F., and Coauthors, 2014: The effect of horizontal resolution on simulation quality in the Community Atmospheric Model, CAM5.1. *J. Adv. Model. Earth Syst.*, **6**, 980–997, https://doi.org/10.1002/2013MS000276.

Wu, Y., S. Chen, W. Li, R. Fang, and H. Liu, 2020: Relative vorticity is the major environmental factor controlling tropical cyclone intensification over the western North Pacific. *Atmos. Res.*, **237**, 104874, https://doi.org/10.1016/j.atmosres.2020.104874.

Xu, K.-M., and D. A. Randall, 1996: A semiempirical cloudiness parameterization for use in climate models. *J. Atmos. Sci.*, **53**, 3084–3102, https://doi.org/10.1175/1520-0469(1996)053<3084:ASCPFU>2.0.CO;2.

Yanai, M., S. Esbensen, and J.-H. Chu, 1973: Determination of bulk properties of tropical cloud clusters from large-scale heat and moisture budgets. *J. Atmos. Sci.*, **30**, 611–627, https://doi.org/10.1175/1520-0469(1973)030<0611:DOBPOT>2.0.CO;2.

Yoo, C., S. Lee, and S. B. Feldstein, 2012: Arctic response to an MJO-like tropical heating in an idealized GCM. *J. Atmos. Sci.*, **69**, 2379–2393, https://doi.org/10.1175/JAS-D-11-0261.1.

Yu, J., T. Li, Z. Tan, and Z. Zhu, 2016a: Effects of tropical North Atlantic SST on tropical cyclone genesis in the western North Pacific. *Climate Dyn.*, **46**, 865–877, https://doi.org/10.1007/s00382-015-2618-x.

——, C. Chen, T. Li, X. Zhao, H. Xue, and Q. Sun, 2016b: Contribution of major SSTA modes to the climate variability of tropical cyclone genesis frequency over the western North Pacific. *Quart. J. Roy. Meteor. Soc.*, **142**, 1171–1181, https://doi.org/10.1002/qj.2722.

Zhang, L., L. Wu, and L. Yu, 2011: Oceanic origin of a recent La Niña-like trend in the tropical Pacific. *Adv. Atmos. Sci.*, **28**, 1109–1117, https://doi.org/10.1007/s00376-010-0129-6.

Zhang, W., G. A. Vecchi, H. Murakami, G. Villarini, T. L. Delworth, X. Yang, and L. Jia, 2018: Dominant role of Atlantic Multidecadal Oscillation in the recent decadal changes in western North Pacific tropical cyclone activity. *Geophys. Res. Lett.*, **45**, 354–362, https://doi.org/10.1002/2017GL076397.

Zhao, H., and C. Wang, 2016: Interdecadal modulation on the relationship between ENSO and typhoon activity during the late season in the western North Pacific. *Climate Dyn.*, **47**, 315–328, https://doi.org/10.1007/s00382-015-2837-1.

——, X. Duan, G. B. Raga, and P. J. Klotzbach, 2018a: Changes in characteristics of rapidly intensifying western North Pacific tropical cyclones related to climate regime shifts. *J. Climate*, **31**, 8163–8179, https://doi.org/10.1175/JCLI-D-18-0029.1.

Zhao, J., R. Zhan, Y. Wang, and H. Xu, 2018b: Contribution of the interdecadal Pacific oscillation to the recent abrupt decrease in tropical cyclone genesis frequency over the western North Pacific since 1998. *J. Climate*, **31**, 8211–8224, https://doi.org/10.1175/JCLI-D-18-0202.1.

Zhao, M., I. M. Held, S.-J. Lin, and G. A. Vecchi, 2009: Simulations of global hurricane climatology, interannual variability, and response to global warming using a 50-km resolution GCM. *J. Climate*, **22**, 6653–6678, https://doi.org/10.1175/2009JCLI3049.1.

Zhao, X., and R. J. Allen, 2019: Strengthening of the Walker Circulation in recent decades and the role of natural sea surface temperature variability. *Environ. Res. Commun.*, **1**, 021003, https://doi.org/10.1088/2515-7620/ab0dab.